Electronic properties of the bilayer nickelates $R_3Ni_2O_7$ with oxygen vacancies (R = La or Ce)

Xuelei Sui,[1,2] Xiangru Han,[2] Heng Jin,[3,2] Xiaojun Chen,[4] Liang Qiao,[5] Xiaohong Shao,[1,*] and Bing Huang[2,3,†]

[1]*College of Mathematics and Physics, Beijing University of Chemical Technology, Beijing 100029, China*

[2]*Beijing Computational Science Research Center, Beijing 100193, China*

[3]*Department of Physics, Beijing Normal University, Beijing 100875, China*

[4]*School of Mechanical Engineering, Chengdu University, Chengdu 610106, China*

[5]*School of Physics, University of Electronic Science and Technology of China, Chengdu 611731, China*

(Received 17 November 2023; revised 14 May 2024; accepted 16 May 2024; published 28 May 2024; corrected 29 July 2024)

The discovery of superconductivity in $La_3Ni_2O_7$ has sparked significant research interest in the field of nickelate superconductors. Despite extensive studies on pristine $La_3Ni_2O_7$, the role of oxygen vacancies (V_O), a common type of intrinsic defect in oxides, on electronic structures and superconductivity in $La_3Ni_2O_7$ remains unclear. In this paper, we identify that the loss of intrabilayer apical oxygen is the most energetically favorable. The electronic structure undergoes notable changes, particularly for the Ni-d_{z2} and Ni-d_{x2-y2} orbitals. The d_{z2} orbital shifts downward, substantially reducing its proportion at the Fermi level. Conversely, the proportion of the d_{x2-y2} state increases due to the orbital localization. Applying the two-band model, the hopping strength between intrabilayer d_{z2} functions is observed to increase significantly but with opposite signs, which deviates from the previous understanding. The interorbital hopping between d_{z2} and d_{x2-y2} functions decreases in the presence of V_O. Our results indicate that the formation of V_O could be harmful to the superconductivity in $La_3Ni_2O_7$, considering the general assumption regarding the critical role of d_{z2} in superconductivity generation. Additionally, we propose that $Ce_3Ni_2O_7$, possessing similar electronic structures to $La_3Ni_2O_7$, could be a promising nickelate superconductor with a potential low concentration of V_O.

DOI: 10.1103/PhysRevB.109.205156

I. INTRODUCTION

Besides the infinite-layer nickelates $RNiO_2$ (R = La, Nd, or Pr) [1–5], Ruddlesden-Popper bilayered perovskite $La_3Ni_2O_7$ (La327) was recently discovered to be another unconventional nickelate-based superconductor [6–10]. In contrast to the low superconducting temperature observed in $RNiO_2$ thin films (e.g., ∼10 K at ambient pressure [1] and ∼30 K at 12.1 GPa [11]), bulk La327 exhibits significantly higher T_c values, reaching up to ∼80 K under 14 GPa [6–8]. Importantly, both monocrystalline and polycrystalline samples are found to be superconducting and undergo a structural phase transition from *Amam* to *Fmmm* (or *I4/mmm*) around 14–15 GPa [8,12–14]. Constructed by NiO_6 bilayers, the basic electronic structure of La327 is characterized by the $3d^{7.5}$ configuration with fully occupied t_{2g} orbitals, the bonding-antibonding molecular d_{z2} state, and the nearly quarter-filled itinerant d_{x2-y2} state [6,15]. The effective models suggest that the significant intraorbital exchange between d_{z2} orbitals, as well as the interorbital hybridization between d_{z2} and d_{x2-y2} orbitals, may play a crucial role in the observed superconductivity [16–26]. Meanwhile, the pairing symmetry [27–30], the role of Hund's coupling [15,31], and the electronic correlation effects of pristine La327 [32–36] are extensively studied. To date, significant differences have been observed between La327 and infinite-layer nickelates, but the consensus regarding the superconductivity mechanism in La327 is still lacking.

In La327 samples, the existence of oxygen vacancies (V_O) is inevitable [6,7,9,37], similar to the situations in many other oxides [38–44]. Experimental investigations have revealed that a significant concentration of V_O ($La_3Ni_2O_{7-\delta}$, where $\delta > 0.08$) can induce phase transitions and even trigger metal-semiconductor transitions under ambient pressure conditions [45–47]. Additionally, certain samples with a higher V_O concentration, for instance, $\delta = 0.65$, exhibit weak ferromagnetism [45]. Particularly, the recently discovered uniformed resistivity in La327 under pressure may be highly related to the presence of oxygen defects [6–10]. To gain a deeper understanding of the relationship between V_O and the electronic properties of La327, it is crucial to investigate the energetically favorable positions of these vacancies and their influences on the electronic structures under varying pressure conditions, which are, however, still lacking. Furthermore, given the fact that different rare-earth elements in infinite-layer nickelates and cuprates are realized [4,48], it is valuable to consider the presence of V_O in various rare-earth bilayered perovskites [27,49–51]. Therefore, the major purpose of this work is to systemically identify the role of V_O in La327 and suggest a possible way via rare-earth replacement to enhance the superconductivity.

In this paper, using first-principles calculations, we systematically explore the impact of V_O on the structures and electronic structures of La327. Our calculations indicate that the removal of inner apical oxygen, which connects the NiO_6

*shaoxh@buct.edu.cn

†bing.huang@csrc.ac.cn

bilayers, is the most energetically favorable for the formation of V_O. The introduction of V_O induces significant changes in the d_{z2} orbital. Specifically, the d_{z2} orbitals of the Ni atoms connected to the V_O become fully occupied, resulting in a substantial decrease in the proportion at the Fermi level. Furthermore, the coupling between intralayer d_{z2} Wannier orbitals in defective Ni dimer is found to be much larger but with opposite signs compared to that in pristine Ni dimer. The interorbital hopping between d_{z2} and d_{x2-y2} Wannier functions reduces when V_O exists. In addition, Ce327 shows a larger V_O formation energy, implying a potentially lower concentration of V_O. Overall, our findings provide valuable insights into the effects of V_O in *R*327 compounds and highlight the potential of Ce327 as a high-T_c superconducting candidate.

II. METHODS

All the lattice relaxations and electronic property calculations are performed using the Vienna *Ab initio* Simulation Package (VASP) [52–54]. The Perdew-Burke-Ernzerhof exchange-correlation functional [55] and projector augmented-wave pseudopotentials [56] are employed, with $4f$ electrons of *R* atoms treated as core electrons. Structure relaxations for both lattice constants and atomic positions are done under all considered pressures. The phonon spectra are calculated using the density-functional perturbation theory implemented in the VASP code and analyzed by the PHONOPY software [57–60]. Computations using the frozen phonon method are also carried out for double checking [61]. The Wannier downfolding via the WANNIER90 code [62] is utilized to obtain onsite energy differences, with La-d, Ni-d, and O-p orbitals considered. The hopping parameters in the two-band model are obtained by downfolding the band structure with Ni-d_{z2} and Ni-d_{x2-y2} orbitals. To achieve consistency with the experimentally measured Fermi surface [63], onsite Hubbard U ($U = 4$ eV) is added to Ni-3d orbitals [64] (see Fig. 8 in the Appendix).

III. RESULTS AND DISCUSSION

A. Structures with V_O

To simplify the analysis and facilitate better comparisons, the conventional cell of La327 with a total of 28 oxygen atoms is investigated, leaving the cases for the 2×2×1 supercell in the Appendix. As seen in previous works, the space group of pristine La327 changes from *Amam* to *I4/mmm* at pressure around 10 GPa [14,29,30]. The nonequivalent O sites for generating V_O in these two phases are labeled in Fig. 1(a). After full structure relaxations, the total energy difference of La327 with one vacancy is given in Fig. 1(b). The lowest energy under each pressure is set as 0; the formation energy of V_{O1} will be discussed later. Interestingly, for both phases, the structures with the loss of the inner bilayer apical oxygen atom [V_{O1}, site 1 in Fig. 1(a)] exhibit the lowest energy. The energies of structures with the loss of outer bilayer apical [V_{O4}, site 4 in Fig. 1(a)] are several electron volts higher, while the energies of structures with in-plane V_{O2} and V_{O3} [sites 2 and 3 in Fig. 1(a)] are ∼0.5 eV higher. The energy differences for La327 with different V_O are comparable to the values reported in other theatrical works [51]. The extremely

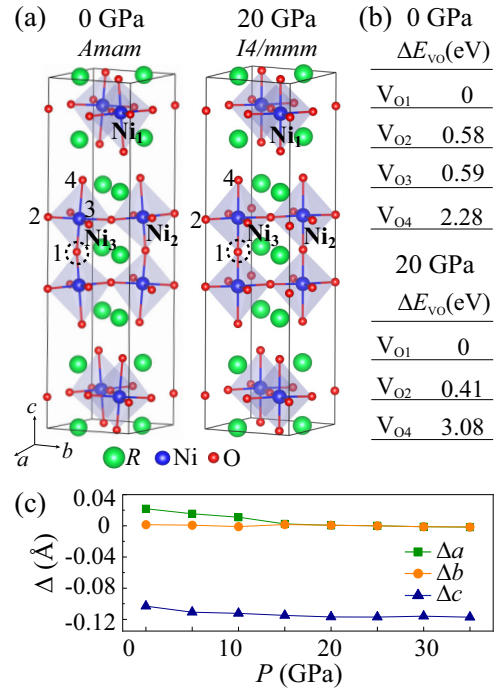

FIG. 1. (a) Schematic crystal structures of *R*327 in the *Amam* phase (0 GPa, left panel) and the *I4/mmm* phase (20 GPa, right panel). The numbers label the nonequivalent oxygen atoms (O_1, O_2, O_3, and O_4). Ni_1 (Ni atoms without V_{O1}), Ni_2 (Ni atoms next to the V_{O1}), and Ni_3 (Ni atoms with V_{O1}) represent three nonequivalent Ni atoms when V_{O1} defect is formed (marked as the dashed circles at site 1). (b) Total energy differences for V_O formed at different positions. Here, the lowest energy (V_{O1}) under each pressure is set as 0. (c) Changes of the lattice constants with V_{O1} defect.

high energy of structure with V_{O2} demonstrated in our work is consistent with the nearly 100% occupation of outer apical oxygen sites. Conversely, structures with V_{O1} exhibit the lowest energy, suggesting the highest formation probability of inner apical oxygen vacancies [37]. Taking La327 under 20 GPa as an example, the introduction of V_{O1} gives rise to three nonequivalent Ni atoms, in terms of their distance to the V_{O1}: Ni_1 is the Ni atom in pristine bilayer NiO_6, Ni_2 is the Ni atom with corner-shared O connecting to NiO_5, and Ni_3 is the Ni atom in NiO_5 environment. The electronic differences of these Ni atoms will be discussed later. As shown in Fig. 1(c), the loss of the apical oxygen atom decreases the lattice constant along the c axis largely, while slightly increasing the lattice constants in the ab plane at 0 GPa. The anisotropic variations in the lattice constants a and b may be related to the ongoing debate regarding the experimentally detected *Fmmm* or *I4/mmm* symmetries [6,13,14]. When the pressure is increased, the changes in lattice constants exhibit slight variations.

B. Electronic properties with apical V_O

Taking the case of La327 with V_{O1} at 20 GPa as an example, the electronic structures contributed by different Ni atoms are projected for comparison. Figure 2(a) provides a sketch of the orbital configurations for Ni_1 (Ni_2) and Ni_3 atoms

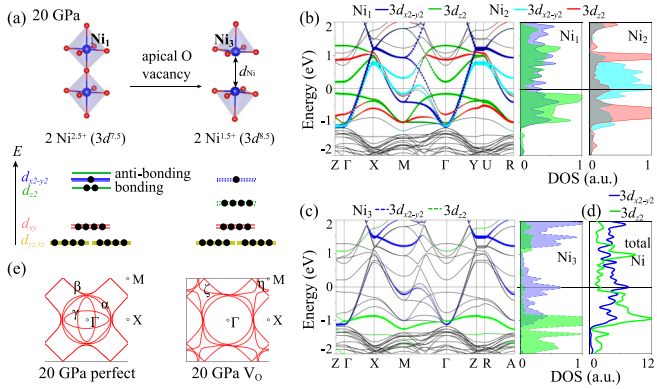

FIG. 2. Electronic structures for La327 with V_{O1} under 20 GPa. (a) Schematic local structures and crystal-field splitting for bilayer without (left panel) and with V_{O1} (right panel). The number of electrons occupying each orbital is denoted by black dots. The distance between two Ni atoms in the dimer is labeled as d_{Ni}. (b) Projected band structures and DOS for Ni_1 and Ni_2 atoms. The E_F is set to zero. (c) Same as (b) but for Ni_3 atoms. (d) Projected DOS of d_{z2} and d_{x2-y2} orbitals for all eight Ni atoms. (e) FSs at 20 GPa for La327 without (left panel) and with (right panel) V_{O1}. The hole pocket γ and electron pocket η, as well as FS sheets of α, β, and ζ are labeled.

[see Fig. 1(a) for the definition of different Ni atoms]. For the Ni_1 atom, the filling of $3d$ electrons is 7.5 in terms of the formal electron count, giving rise to $Ni^{2.5+}$. The strong hybridization with intrabilayer apical O splits the d_{z2} into a bonding-antibonding molecular-orbital state. In the presence of oxygen vacancies, the Ni_3 atom is in the pyramidal environment. In this scenario, the e_g orbitals are fully occupied, similar to the case of Ni_1. Notably, the d_{z2} orbital in the pyramidal environment exhibits lower energy than the d_{x2-y2} orbital, which becomes fully filled. The total $3d$ filling of Ni_3 is 8.5, resulting in $Ni^{1.5+}$. The distance between two Ni atoms in one bilayer, denoted as d_{Ni}, is measured to be 3.38 Å for Ni_3 dimer, significantly smaller than those of Ni_1- (3.82 Å) and Ni_2 dimers (3.71 Å). (At 0 GPa, the distance between two Ni atoms ($d_{Ni} = 3.78$ Å) decreases to 3.51 Å upon the loss of apical oxygen, consistent with the experimentally observed ∼0.2-Å reduction of d_{Ni} at $\delta = 0.34 \pm 0.22$ [14]). For all Ni atoms, the filling of the in-plane orbitals remains similar, with the t_{2g} orbitals being fully occupied and the d_{x2-y2} orbital nearly quarter filled.

To better understand the contributions of different Ni atoms to the electronic structure of La237, the d_{x2-y2} and d_{z2} orbitals for Ni_1, Ni_2, and Ni_3 are projected separately, as illustrated in Figs. 2(b) and 2(c). It is observed that the t_{2g} orbitals are always fully occupied below the Fermi level. The following differences between three Ni atoms can be observed: (1) For Ni_1 atoms, the band dispersions of the Ni_1-d_{z2} and Ni_1-d_{x2-y2} orbitals resemble those of Ni atoms in the pristine case (see Fig. 9 in the Appendix). However, the introduction of V_{O1} breaks the inversion symmetry, separating the energy levels of Ni_1-d_{z2} from those of Ni_2 and Ni_3. The energy splitting of the bonding-antibonding states of Ni_1-d_{z2} increased, as evidenced at the Z- and Γ points in Fig. 2(b), which is similar to the situation of $La_3Ni_2O_{6.75}$ at 0 GPa reported in a recent work [51]. (2) For Ni_2 atoms, the smaller distance between Ni_2 dimer (d_{Ni2}) leads to an enhanced σ-bond coupling through O-p_z compared to that of Ni_1-d_{z2}. This stronger coupling gives rise to a more localized Ni_2-d_{z2} orbital and a larger energy splitting of the bonding-antibonding states, as demonstrated in the projected density of states (DOS) in the right panel of Fig. 2(b). Moreover, the band dispersion of Ni_2-d_{x2-y2} reduces largely, leading to a large proportion around E_F. (3) For Ni_3 atoms, the d_{z2} orbitals are fully occupied and experience a significant downward-energy shift, approaching the energy levels of the t_{2g} orbitals. Meanwhile, the energy of Ni_3-d_{x2-y2} shifts upwards slightly, accompanied by a small decrease in orbital filling. Therefore, the formation of V_{O1} significantly renormalizes the electronic structure around the Fermi level.

Figure 2(d) gives the sum of DOS for all eight Ni atoms in La327 with V_{O1}. Compared to the large proportion of bonding states of d_{z2} at E_F for the pristine case [see Fig. 9(a) in the Appendix], the d_{z2} shifts away with a much lower proportion around E_F for the V_O case. Meanwhile, the proportion of d_{x2-y2} orbital around E_F increases significantly, even surpassing the proportion of the d_{z2} state [65]. This is different from the pristine case, where the d_{z2} orbital has a much larger proportion than the d_{x2-y2} orbital. Consequently, the total DOS of Ni-3d orbital around E_F decreases with the inclusion of V_O. The Fermi surfaces (FSs) of La327 without and with V_{O1} are illustrated in Fig. 2(e) for comparison. For the pristine case, the observed hole pocket γ (primarily composed of d_{z2} orbital) as well as the FS sheets α and β (a mixture of d_{z2} and d_{x2-y2} orbitals) are consistent with the previous works [17,24,65]. When V_{O1} exists, the FS sheets α and β remain almost unchanged while the hole pocket γ disappears due to the strong downward energy shift of d_{z2}. In addition, the electron pocket η around the M point and FS sheet ζ emerges, which is mainly composed of d_{x2-y2} orbitals originating from Ni_2 and Ni_3 atoms. It is reported that the γ pocket plays a decisive role in superconductivity by significantly contributing to the random-phase approximation (RPA)-renormalized spin susceptibility matrix, facilitating energy gain, and participating in interlayer pairing [24]. Therefore, the disappearance of the γ pocket due to oxygen vacancies could be detrimental to superconductivity. Furthermore, the inhomogeneous distribution of V_{O1} may induce the inhomogeneous superconducting properties in the samples.

It is interesting to further understand the evolution of electronic properties with V_{O1} under increased pressures, as illustrated in Fig. 3. The projected DOS is contributed by the combination of all eight Ni atoms in the conventional cell. As pressure increases, the bonding state of Ni_1-d_{z2} shifts upward (as indicated by the red points), similar to the behavior observed in pristine La327. In contrast, the energy level of the bonding state of Ni_2-d_{z2} remains almost unchanged (the magenta points), while the energy level of the antibonding state of Ni_2-d_{z2} increases with increasing pressure (the orange points). The d_{x2-y2} orbital around E_F experiences minimal changes as pressure increases, while E_F always crosses the peak position of the d_{x2-y2} orbital for all pressures.

C. Orbital interactions with V_O

The minimal two-band model, consisting of d_{z2} and d_{x2-y2} orbitals, has been proposed to describe the electronic

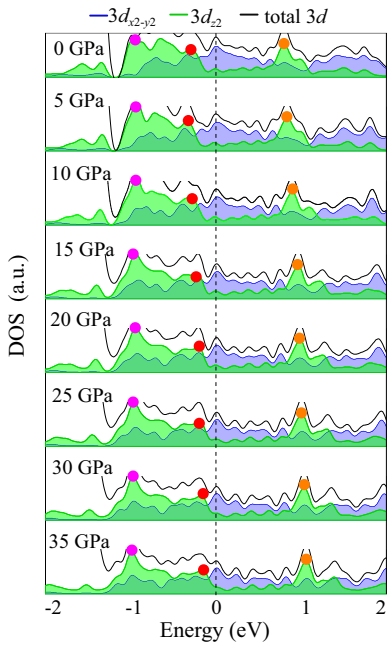

FIG. 3. Projected DOS of d_{z2} and d_{x2-y2} orbitals for the sum of eight Ni atoms in La327 with V_{O1}. The orange, red, and magenta points represent the peak positions contributed mainly by the antibonding Ni_2-d_{z2} states, bonding Ni_1-d_{z2} states, and the combination of Ni_3-d_{z2} and bonding Ni_2-d_{z2} states, respectively.

properties of pristine La327. Research shows that the substantial intraorbital coupling of d_{z2} orbitals along the c axis (t_c^z), together with the large interorbital hybridization between d_{z2} and itinerant d_{x2-y2} orbitals along the a axis (t_a^{zx}), may play a crucial role in achieving high-T_c superconductivity [17,25,26]. To investigate the effects of V_{O1} on these critical orbital interactions, the changes in the model parameters are analyzed based on maximally localized Wannier functions (MLWFs) [66]. The band structures, hopping integrals, and plots of Wannier orbitals are done by postprocessing. All orbitals around E_F are utilized to fit the band structure and decide the energy position of each orbital, including La-5d, Ni-3d, and O-2p, as depicted in Fig. 4(a). To further explicitly demonstrate the parameter changes in the minimal two-band model, the full band structure is downfolded to a noninteracting model based on d_{z2} and d_{x2-y2} orbitals, as illustrated in Fig. 4(b). The FSs (for both $k_z = 0$ and $k_z = \pi$ sections) obtained from the two-band model are illustrated (see Fig. 10) in the Appendix. The excellent agreement between the band structures and FSs derived from the Wannier downfolding and those obtained from the density-functional theory (DFT) calculations confirms the faithful transformation to MLWFs.

The MLWFs downfolded by d_{x2-y2} and d_{z2} orbitals for three Ni atoms are given in Figs. 4(c)–4(e). The d_{x2-y2}-like functions, which are formed by a combination of d_{x2-y2} and O-p_x/p_y orbitals, are similar among three nonequivalent Ni atoms and also resemble the non-V_O case [18]. On the other hand, the d_{z2}-like functions for Ni_1 and Ni_2 atoms are combined by d_{z2} and O-p_z, exhibiting a strong σ-bonding character through the involvement of O-p_z orbitals. However, the d_{z2}-like function for Ni_3 is notably different, as it captures a significant contribution from the s orbital of residual electrons caused by the loss of oxygen atoms (see the band projection for the s orbital in Fig. 11 in the Appendix). The phases of d_{z2}-like functions are also labeled, demonstrating different parity for Ni_1 (Ni_2) and Ni_3 atoms; their interactions on hopping strength will be discussed later.

Figures 5(a) and 5(b) illustrate the schematic diagrams of Ni bilayer structures without and with V_{O1}, respectively. Noticeable lattice distortion is observed in Fig. 5(b). Without V_{O1}, the distance between Ni_1-Ni_1 atoms d_{Ni1} is 3.82 Å. The absence of apical oxygen leads to a notable reduction in d_{Ni3} (3.38 Å) as well as a decrease in d_{Ni2} (3.71 Å). As shown in Fig. 5(c), the crystal-field splittings for Ni_1 and N_2 atoms are fairly close but significantly differ from that of Ni_3. The energy difference between d_{x2-y2} and d_{z2} orbitals (ε_1) is observed to be lower in Ni_2 than in Ni_1, which is attributed to the downward energy shift of Ni_2-d_{x2-y2} orbital, as shown in Fig. 2(b). As pressure increases, ε_1 for both Ni_1 and Ni_2 decrease due to the upward energy shift of the antibonding d_{z2} state. However, for Ni_3 with fully occupied d_{z2} states, ε_1 is significantly larger than that in Ni_1 and Ni_2. With increasing pressure, ε_1 for Ni_3 remains almost constant, which is reflected by the unchanged energy level of Ni_3-d_{z2} orbital (Fig. 3). The energy difference between d_{z2} and t_{2g} orbitals (ε_2) is slightly higher in Ni_2 than in Ni_1, and both values increase with pressure. However, ε_2 for Ni_3 are much smaller, even smaller than ε_1 for Ni_3. In addition, the loss of

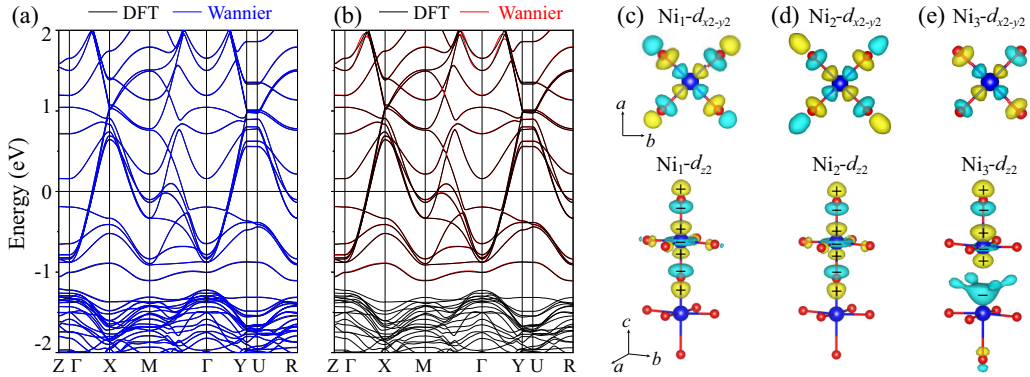

FIG. 4. (a) Wannier fitting based on Wannier orbitals of La-5d, Ni-3d, and O-2p for La327 with V_{O1}. (b) Wannier fitting based on Wannier orbitals of d_{x2-y2} and d_{z2}. d_{x2-y2}-like and d_{z2}-like Wannier functions with phases labeled for (c) Ni_1, (d) Ni_2, and (e) Ni_3 atoms.

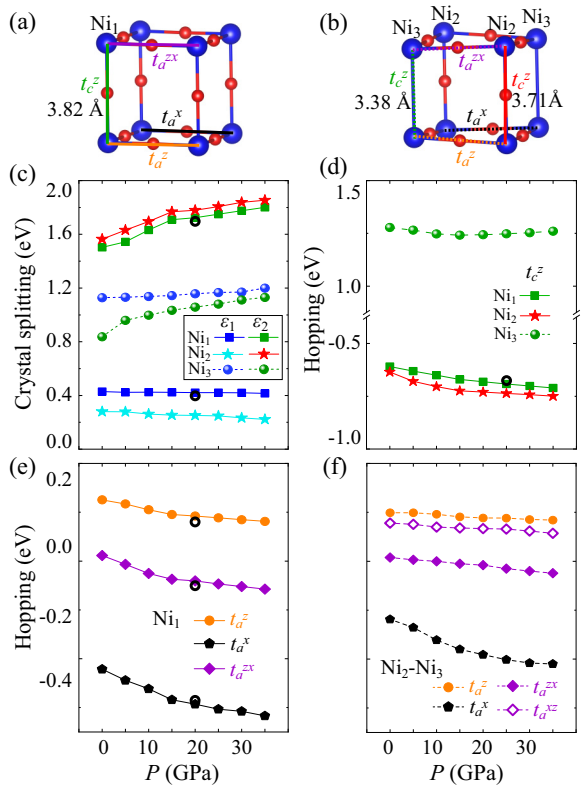

FIG. 5. Onsite energy differences and hopping parameters for three nonequivalent Ni atoms in La327 with V_{O1}. Sketch of the Ni bilayer structures (a) without and (b) with V_{O1}. The distances between two Ni atoms along the c axis (d_{Ni}) are labeled. The hopping parameters are labeled by colored lines: t_c^z (green, NN coupling between intrabilayer d_{z2} along c axis); t_a^z (orange, NN coupling between d_{z2} along a axis); t_a^x (black, NN coupling between d_{x2-y2} along a axis); and t_a^{zx} (purple, NN coupling between d_{z2} and d_{x2-y2} along a axis). (c) Crystal-field splitting ε_1 (between d_{x2-y2} and d_{z2} orbitals) and ε_2 (between d_{z2} and t_{2g} orbitals) for three nonequivalent Ni atoms as a function of pressure. (d) t_c^z as a function of pressure. (e) t_a^z, t_a^x, and t_a^{zx} for Ni_1 atom as a function of pressure. (f) Same as (e) but for the hoppings between orbitals of Ni_2 and Ni_3 atoms. Note that the hopping strength between Ni_2-d_{z2} and Ni_3-d_{x2-y2} (t_a^{zx}, represented by solid purple rhombus) is different from the hopping strength between Ni_2-d_{x2-y2} and Ni_3-d_{z2} (t_a^{xz}, represented by hollowed purple rhombus). The black circles in (c)–(e) represent the values for the parameter in pristine La327 under 20 GPa, which are close to the corresponding symbols of Ni_1.

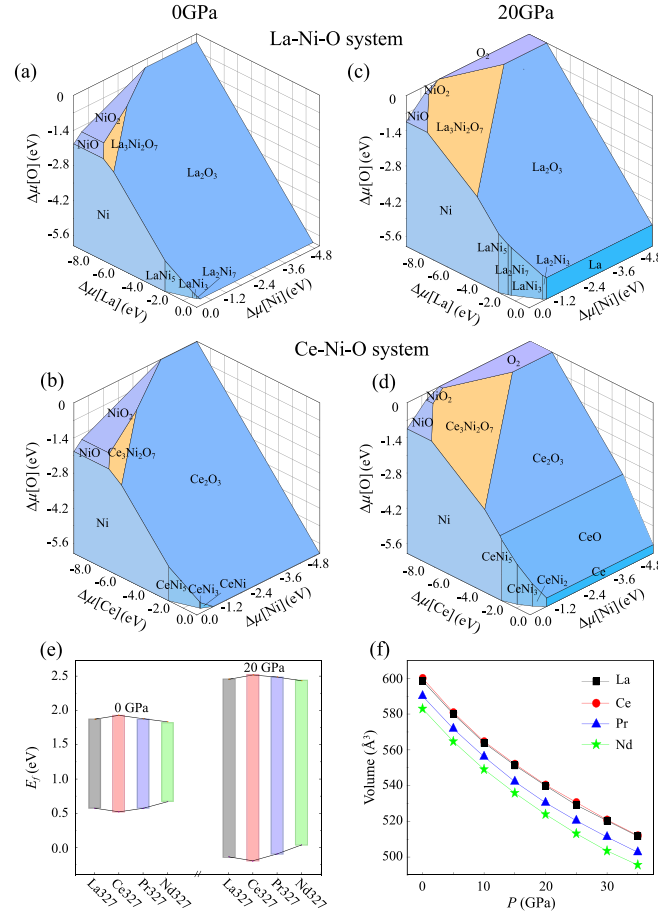

FIG. 6. Phase diagrams for (a), (c) La-Ni-O and (b), (d) Ce-Ni-O systems under 0 and 20 GPa. The stable chemical-potential region is highlighted in orange. (e) Formation energies (E_f) of apical oxygen vacancies for R327 under 0 and 20 GPa. (f) The change of volume for pristine R327 under pressure.

the oxygen atom has minimal impact on the orbital alignment of Ni_1 compared to the Ni atom in pristine La327, as inferred from the comparable onsite energy differences [black circles in Fig. 5(a)] as well as the similar projected band structures [Figs. 2(b) and 9].

Next, the crucial orbital interactions in the two-band model are discussed. The out-of-plane nearest-neighbor (NN) σ-bonding coupling t_c^z is presented in Fig. 5(d). For indirect hopping of d_{z2} through O-p_z in the Ni_1 dimer, t_c^z is proportional to $-(t_c^{zp})^2/\Delta^{zp}$. Here, t_c^{zp} (Δ^{zp}) is the coupling strength (the energy difference) between d_{z2} and O-p_z. The t_c^z value for the Ni_2 dimer is slightly larger than that of the Ni_1 dimer, attributed to the smaller distance; thus, there is larger t_c^{zp} between the Ni_2 and O orbitals. Both t_c^z values for the Ni_1- and Ni_2 dimer increase with pressure. However, the situation is significantly different for t_c^z of Ni_3 atoms, where the apical O-p_z orbital is absent. The coupling strength between Ni_3-d_{z2} functions is significantly enhanced with a positive value. As depicted in Fig. 4(e), the d_{z2}-like Wannier function for Ni_3 captures a significant contribution from the residual s orbital. The band projection in Fig. 11(a) clearly illustrates the distribution of the residual s orbital around E_F. The projected DOS in Fig. 11(b) also reveals a significant overlap between the residual s orbital and the Ni_3-d_{z2} orbital [refer to the projected DOS of Ni_3-d_{z2} in Fig. 2(c)]. Specifically, along the c axis, the p_z orbital exhibits odd parity (polarized), while the residual s orbital demonstrates even parity (unpolarized). Since either the p_z or the residual s orbital incorporates into the d_{z2}-like Wannier orbital, the parity of the d_{z2}-like function is different for Ni atom without and with V_O [Figs. 4(c)–4(e)]. Consequently, this difference in parity symmetry results in an opposite sign of the hopping strength t_c^z. Meanwhile, the great enhancement of t_c^z is mainly attributed to the reduced distance between Ni_3-Ni_3 atoms ($d_{Ni3} = 3.38$ Å), which is much smaller than that of d_{Ni1}(3.82 Å) and d_{Ni2}(3.71 Å).

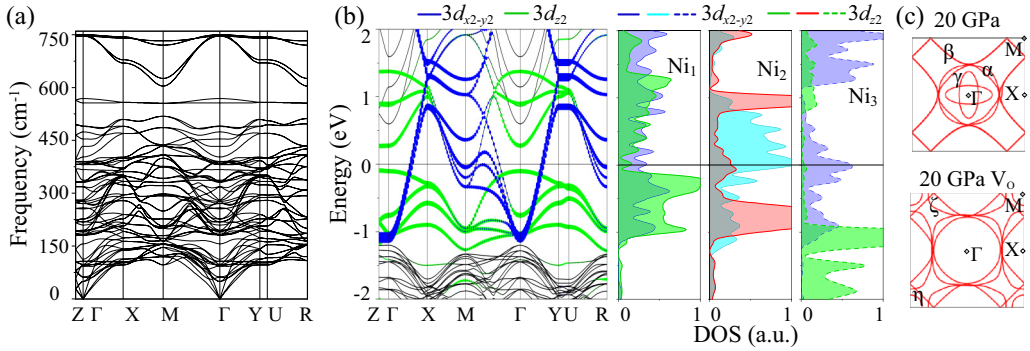

FIG. 7. (a) Phonon spectrum for pristine Ce327 under 20 GPa. (b) Projected band structure with d_{x2-y2} and d_{z2} for all Ni atoms (left panel) and projected DOS for three nonequivalent Ni atoms separately (right panel) for Ce327 under 20 GPa with V_{O1}. (c) FSs for Ce327 without (upper panel) and with V_{O1} (left panel).

Regarding the in-plane orbital couplings shown in Fig. 5(e), the values for Ni_1 orbitals are similar to those of the Ni atom in pristine La327 (black circles). The intraorbital coupling between NN Ni-d_{x2-y2} Wannier functions (t_a^x) is substantial, with a value exceeding 0.4 eV. The interorbital coupling between NN d_{z2} and d_{x2-y2} (t_a^{zx}) is considerable, while the intraorbital coupling of NN d_{z2} along the a axis (t_a^z) is relatively small. All these coupling strengths increase with pressure. For the case with V_{O1}, Ni_3 is adjacent to Ni_2 [Fig. 5(b)], and the in-plane orbital coupling strengths are given in Fig. 5(f). The coupling between Ni_2-d_{z2} and Ni_3-d_{z2} along the a axis (t_a^z) is similar to the value observed in Ni_1-d_{z2}, while the coupling between Ni_2-d_{x2-y2} and Ni_3-d_{x2-y2} (t_a^x) is slightly smaller compared to Ni_1-d_{x2-y2}. The most significant change occurs in the interorbital coupling between d_{z2} and d_{x2-y2} along the a axis between Ni_2 and Ni_3 atoms. The hopping strengths of t_a^{zx} (representing the coupling between Ni_2-d_{z2} and Ni_3-d_{x2-y2}) and t_a^{xz} (representing the coupling between Ni_2-d_{x2-y2} and Ni_3-d_{z2}) demonstrate nonequal values. The NN d_{z2} and d_{x2-y2} orbitals interact through the O-$p_{x/y}$ orbital. This is evidenced by the reduced O-$p_{x/y}$ contribution to the Ni_3-d_{z2}-like function [Fig. 4(e)]; the coupling between Ni_3-d_{z2} and O-$p_{x/y}$ is smaller than that between Ni_2-d_{z2} and O-$p_{x/y}$ (also refer to Fig. 12 in the Appendix). This leads to a smaller t_a^{zx} (around -0.13 eV) value than t_a^{xz} (around -0.21 eV). Moreover, similar to the case in Ni_1, these in-plane interactions between Wannier functions centered at Ni_2 and Ni_3 atoms also increase with pressure. Given that the symmetry of the d_{z2}-like Wannier functions along the a axis remains consistent for Ni atoms without and with V_O, the coupling between two d_{z2} functions along the a axis (t_a^z), as well as the coupling between d_{z2} and d_{x2-y2} functions along the a axis (t_a^{zx} and t_a^{xz}), retain the same sign for different Ni atoms [Figs. 5(e) and 5(f)].

Previous works highlighted the important role of intraorbital coupling of d_{z2} orbitals and the interorbital hybridization between d_{z2} and d_{x2-y2} orbitals in achieving high-T_c superconductivity. Therefore, the significantly enhanced but completely opposite value of t_c^z, along with the notable downward energy shift of the d_{z2}-like Wannier orbital when apical oxygen is lost [Fig. 5(a)], could be detrimental to superconductivity. We note that a recent theoretical study assumes zero intrabilayer coupling between Ni_3-d_{z2} (t_c^z) and the absence of apical oxygen. This assumption could lead to enhanced Fermi-surface nesting, resulting in reduced interaction strength and the emergence of local magnetic moments [28]. However, our results demonstrate the intrabilayer coupling between Ni_3-d_{z2} is enhanced but with an opposite sign [Fig. 5(d)]. Therefore, further investigation is necessary to explore how the changes in orbital interactions within this two-band model affect superconducting properties.

D. Stability of $R_3Ni_2O_7$ and formation energies of V_{O1}

To explore the stability of bilayer nickelate and determine the formation energy of V_{O1}, phase diagrams of the La-Ni-O system are constructed using the CHESTA code [67], as depicted in Figs. 6(a) and 6(c). It is expected that La327 is stabilized in a chemical potential region without the formation of possible competitive phases (e.g., LaO_2, La_2O_3, NiO, NiO_2, La_2Ni_7, $LaNi_5$, La_7Ni_{16}, La_3Ni, LaNi, $LaNi_3$, etc). The narrow, stable chemical-potential region under 0 GPa, highlighted in orange in Fig. 6(a), reflects the challenge of achieving high-quality samples experimentally [6–9,37,51]. Furthermore, the phase diagram under 20 GPa is provided, revealing an expanded stable region and enhanced stability of La327, which may be related to the high symmetry under pressure (*I4/mmm*).

The formation energies (E_f) of single V_{O1} in the La327 conventional cell can be evaluated as

$$E_f = E[La_{12}Ni_8O_{27}] + \mu[O] - E[La_{12}Ni_8O_{28}], \quad (1)$$

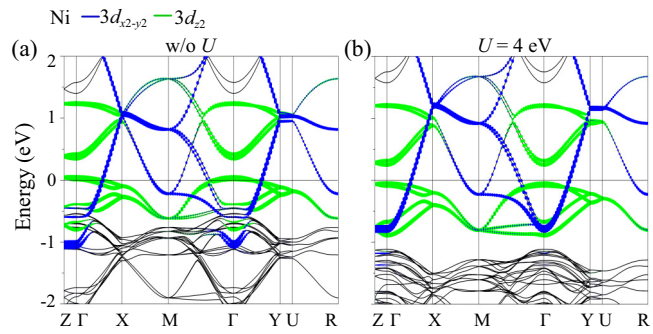

FIG. 8. Projected band structures (a) without and (b) with the consideration of Hubbard U (U = 4 eV) for pristine La327 under 0 GPa for spin-nonpolarized calculations.

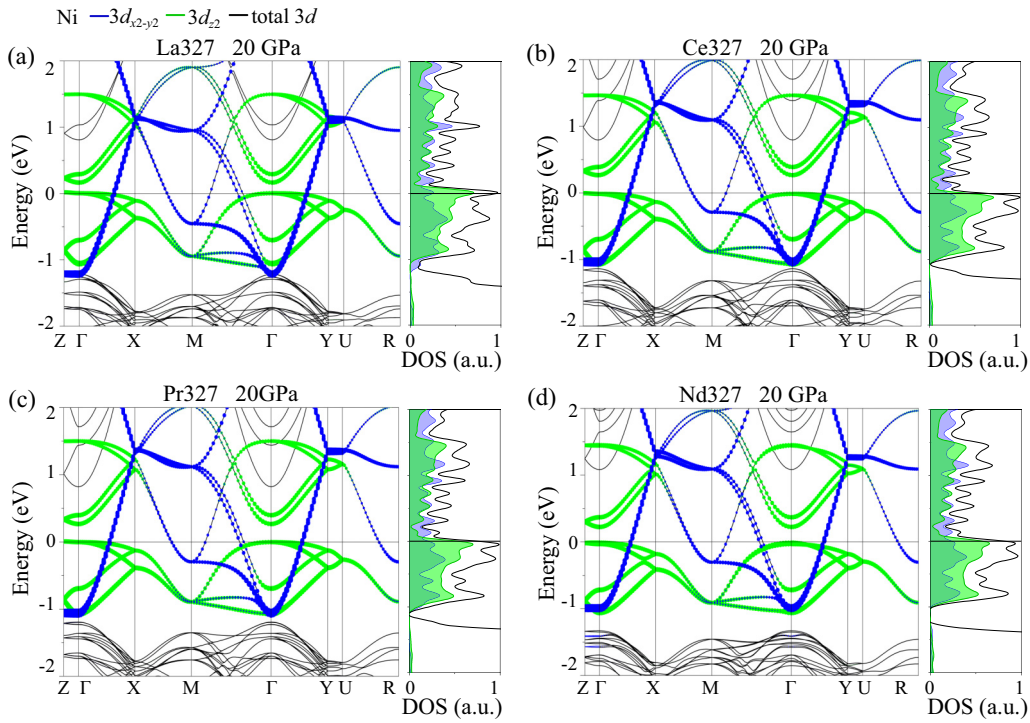

FIG. 9. Projected band structures and DOS for *R*327 under 20 GPa. (a) La327, (b) Ce327, (c) Pr327, and (d) Nd327.

where $E[La_{12}Ni_8O_{27}]$ and $E[La_{12}Ni_8O_{28}]$ are the total energies of $La_{12}Ni_8O_{27}$ and $La_{12}Ni_8O_{28}$, respectively. μ[O] is the chemical potential of oxygen. From the phase diagrams, the chemical-potential range $\Delta\mu$[O] for stable La327 is [−0.96, −2.25] eV and [0, −2.59] eV under 0 and 20 GPa. Thus, the corresponding E_f falls in the ranges of [0.57, 1.86] eV and [−0.13, 2.46] eV at 0 and 20 GPa, respectively, as shown in Figs. 6(e) and 6(f).

Because different rare-earth elements in infinite-layer nickelates and cuprates are realized, as well as the successful synthesis of $La_2PrNi_2O_7$ [4,48,49], it is valuable to investigate the properties of various rare-earth bilayer perovskites, as has been done in other theoretical works [30,50,68]. The phase diagrams of Ce327 are given in Figs. 6(b) and 6(d). The stable chemical-potential region for Ce327 is broader than La327 under both 0 and 20 GPa. Comparison calculations for Pr327 and Nd327 are also conducted (Fig. 13 in the Appendix), showing narrower stable chemical regions than La327. The largest stable region of Ce327 may be related to the larger volume and *c*/*a* value (Fig. 14 in the Appendix). The broader, stable chemical-potential region of Ce327 makes it a promising candidate for bilayer nickelate superconductors. The comparable band structure and FS (as shown in Fig. 9 in the Appendix) for pristine *R*327, combined with the similar pairing strength calculated by the multiorbital RPA model [30], indicate the possibility of superconductivity in Ce327.

We should note that DFT calculations may underestimate the stability of certain perovskites [69,70]. Additionally, the chemical potential μ[O] is influenced by experimental growth conditions, including temperature, which cannot be considered in DFT calculations. Therefore, determining the formation energy accurately is challenging. Nevertheless, the relative values among different systems and the variation trends under pressure remain meaningful.

E. Electronic properties of Ce327 with V_O

Next, the electronic properties of Ce327 with V_{O1} are investigated. Similar to the case in La327, pristine Ce327 undergoes a phase transition from *Amam* to *I*4/*mmm* at around 11 GPa [30]. Figure 7(a) depicts the phonon spectrum for the primitive cell of Ce327 in the *I*4/*mmm* phase at 20 GPa. The absence of imaginary frequencies suggests its thermodynamic stability. The band structure with d_{x2-y2} and d_{z2} orbitals projected for all eight Ni atoms in the presence of V_{O1} is shown in the left panel of Fig. 7(b), and the projected DOS for the three nonequivalent Ni atoms are displayed in the right panel of Fig. 7(b). The definitions of Ni_1, Ni_2, and Ni_3 are the same as those in La327 [Fig. 1(a)]. Interestingly, it is evident that the band structures of Ce327 and La327 exhibit striking similarities, not only in their pristine structures (Fig. 9) but also in the structures with V_{O1} (Fig. 2). When considering the orbital variations of Ni atoms separately, the introduction of V_{O1} has a slight influence on the orbital dispersion but shifts the Ni_1-d_{z2} orbital downward away from E_F. Additionally, the Ni_2-d_{z2} orbital becomes more localized, while the DOS of d_{x2-y2} around E_F increases significantly. For the Ni_3 atom, the d_{z2} orbital is fully occupied, accompanied by a slight upward shift of the d_{x2-y2} orbital. The vanishing of the γ pocket and the appearance of hole pocket η and FS sheet ζ [Fig. 7(c)] are the same as the case in La327 [Fig. 2(e)]. The electronic properties of Pr327 and Nd327 with V_{O1} are presented in Fig. 15 in the Appendix, displaying similar characteristics to those observed in La327. Therefore, possessing comparable electronic structures but

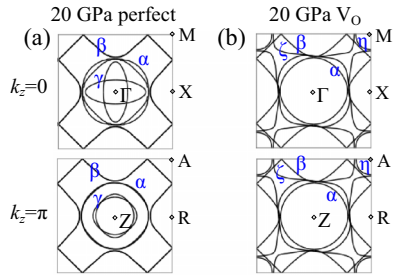

FIG. 10. FSs obtained from the two-band model (a) without and (b) with oxygen vacancies for La327 under 20 GPa. The upper and lower panels are FSs for $k_z = 0$ and $k_z = \pi$ sections, respectively.

potentially low oxygen-vacancy concentration, Ce327 could be a promising candidate for achieving nickelate-based high-T_c superconductors.

F. Discussion and conclusion

It is worth noting that the concentration of V_O considered in our study is relatively high ($R_3Ni_2O_{6.75}$, $\delta = 0.25$). Experimentally, the concentration of oxygen vacancy affects the metallicity of $La_3Ni_2O_{7-\delta}$. Samples exhibit semiconducting behavior when δ>0.08 [45,46]. This behavior is closely related to the formation of charge and spin ordering, which is confirmed experimentally [12,71,72]. However, when pressure is applied, the charge- and spin-density waves diminish rapidly, and therefore they are not considered in our calculations [9,73,74]. Furthermore, our calculations do not account for the potential distribution patterns of oxygen vacancies, which could also impact the electronic structure of $La_3Ni_2O_{6.75}$. In addition, we also consider the structure with a lower V_O concentration. As demonstrated in Fig. 16 in the Appendix, one oxygen vacancy is introduced in the 2×2×1 supercell, resulting in $R_3Ni_2O_{6.9375}$ with $\delta = 0.0625$. The introduction of V_{O1} gives rise to different local environments for the Ni atoms, and the primary electronic properties for each nonequivalent Ni atom are similar to those observed in $R_3Ni_2O_{6.75}$. Specifically, the DOS for d_{z2} around E_F decreases, while the DOS for d_{x2-y2} slightly increases, as the

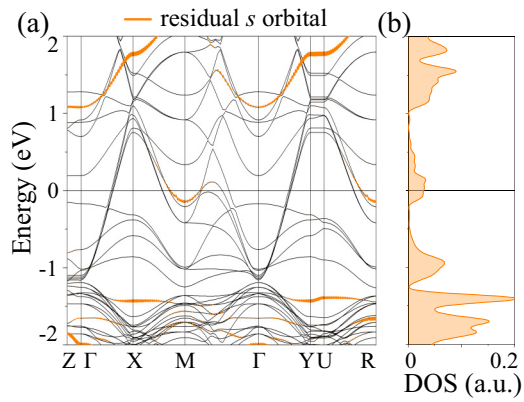

FIG. 11. Projected (a) band structure and (b) DOS for the residual *s* orbital. The band projection is enlarged by ten times to guide the eyes.

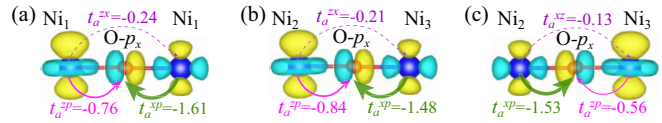

FIG. 12. Hopping paths of the interorbital couplings (a) between Ni_1-d_{z2} and Ni_1-d_{x2-y2} ($t_a^{zx} = t_a^{xz}$), (b) between Ni_2-d_{z2} and Ni_3-d_{x2-y2} (t_a^{zx}), and (c) between Ni_2-d_{x2-y2} and Ni_3-d_{z2} (t_a^{xz}) through O-$p_{x/y}$. The line thickness represents the hopping strength (in units of eV).

case in $R_3Ni_2O_{6.75}$. Therefore, the influences of oxygen vacancies on electronic properties are consistent across varying concentrations. Moreover, it is crucial to acknowledge that the research on bilayer nickelate superconductivity is still in its early stages. Further investigations, such as employing the Hubbard-*U* model [17], *t*-*J* model [20,26,31], and many-body studies [33], are necessary to better understand the impact of oxygen vacancies on superconductivity. It should be noted that the formation of oxygen vacancies is a complex process, and the formation energy serves as one aspect to evaluate the possibility of vacancy formation. In practice, the formation of vacancy is a dynamic process influenced by various factors, including oxygen partial pressure, sample preparation methods, growth rate, and so on. Meanwhile, the ionic radius of Ce is different from La; thus, the octahedral rotations and the valance state of Ce may be different from La, as demonstrated in another theoretical work [50]. Thus, the structure transition and superconductivity properties of Ce327 under pressure need further experimental and theoretical investigations.

In conclusion, our first-principles calculations demonstrate that the most energetically favorable site for the formation of oxygen vacancy in *R*327 is the apical octahedral oxygen connecting NiO_6 bilayers. The formation of oxygen

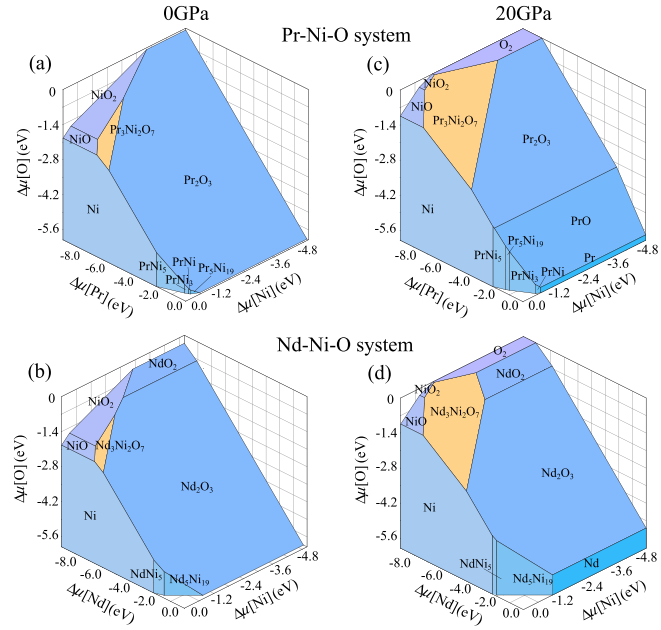

FIG. 13. Phase diagrams for (a), (c) Pr-Ni-O and (b), (d) Nd-Ni-O systems under 0 and 20 GPa. The stable chemical-potential region is highlighted in orange.

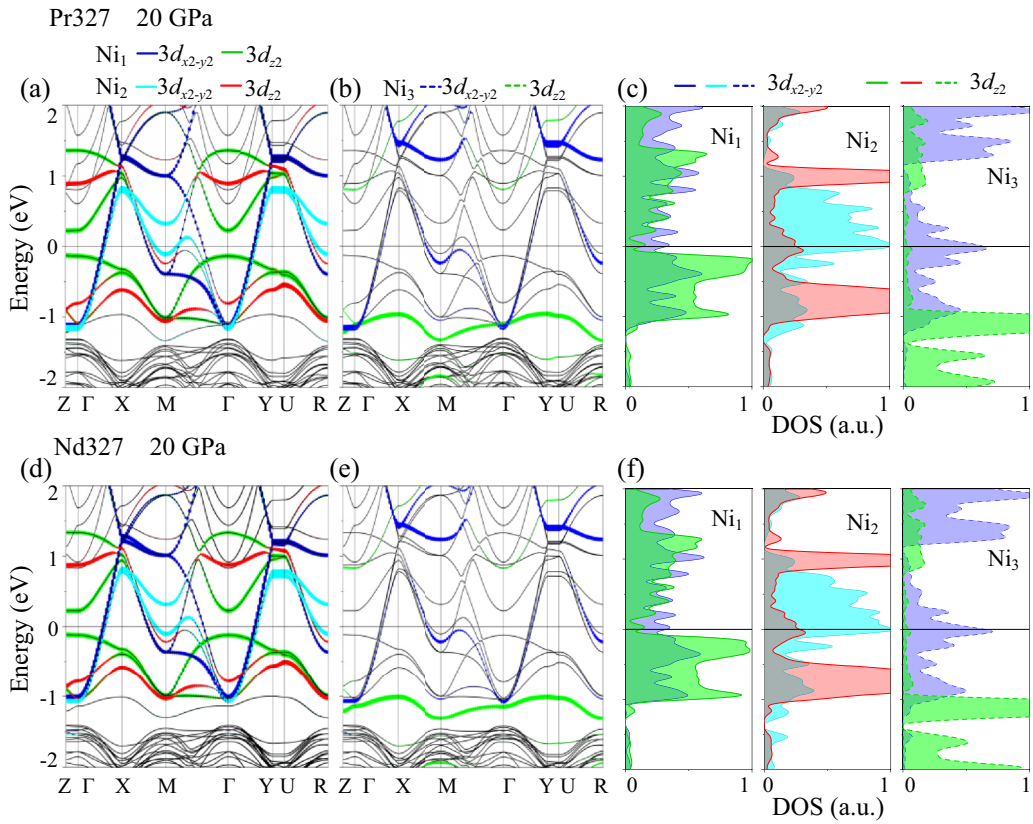

FIG. 14. Electronic properties of Pr327 and Nd327 with V_{O1} under 20 GPa. Projected band structures of (a) Ni_1 and Ni_2, and (b) Ni_3 for Pr327. (c) Projected DOS for Ni_1, Ni_2, and Ni_3 atoms for Pr327. Projected band structures of (d) Ni_1 and Ni_2, and (e) Ni_3 for Nd327. (f) Projected DOS for Ni_1, Ni_2, and Ni_3 atoms for Nd327.

vacancies leads to an increased filling of the d_{z2} orbital, significantly reducing its proportion at E_F. Simultaneously, the orbital hopping strength between nearest-neighbor d_{z2}-like functions along the c axis increases significantly but with an opposite sign. Additionally, the interorbital coupling between d_{z2} and d_{x2-y2} is reduced because of the weakened coupling between d_{z2} and $p_{x/y}$. These alterations in d_{z2} orbitals caused by oxygen vacancies could potentially be harmful to the superconductivity in $R327$, as the metallic d_{z2} orbitals play a decisive role in the emergence of superconductivity. Moreover, holding similar electronic properties but a larger lattice volume, we suggest that Ce327 is a promising candidate for high-T_c superconductivity with possible lower V_O concentrations.

ACKNOWLEDGMENTS

This work is supported by the Fundamental Research Funds for the Central Universities (Grant No. buctrc202402), National Key Research and Development of China (Grant No. 2022YFA1402401), NSFC (Grant No. 12088101), and NSAF (Grant No. U2230402). Computations were done at the Tianhe-JK supercomputer at CSRC.

APPENDIX

Comparing Figs. 8(a) and 8(b), the band dispersion and the energy position of d_{x2-y2} as well as the antibonding d_{z2} state show slight variations. However, the energy position of the bonding d_{z2} state shifts downwards upon applying U. The hole pocket (γ pocket) around the Γ point lying below the Fermi level in the $U = 4$ eV case is consistent with the FS observed via synchrotron-based angle-resolved photoemission spectroscopy [58]. In contrast, the hole pocket around the Γ point crossing the Fermi level in the $U = 0$ case contradicts the experimental findings. These results highlight the necessity of incorporating Hubbard U to accurately calculate the electronic properties of $R327$, even in the absence of spin polarization.

The band structures and DOS for $R327$ given in Fig. 9 are similar to the previous works. The FSs obtained from the two-band model without and with oxygen vacancies for La327 under 20 GPa are given in Fig. 10. The model reproduces the FSs in Fig. 2(e) well. When comparing the FSs for the $k_z = 0$ and $k_z = \pi$ sections in Fig. 10(a), slight variations in the γ pocket are observed, while the α- and β pockets remain mostly unchanged. With the introduction of V_{O1}, as given in Fig. 10(b), the γ pocket shrinks and ζ- and η pockets emerge. In this case, the FSs for $k_z = 0$ and $k_z = \pi$ are identical. That is, the γ pocket, composed dominantly of the d_{z2} orbital, displays three dimensionality. The α-, β-, ζ-, and η pockets, involving a mixture of d_{x2-y2} and d_{z2} orbitals, appear predominantly two dimensional.

The projected band structure and DOS for the residual s orbital are given in Fig. 11, demonstrating the proportion of residual s orbital clearly. The NN d_{z2} and d_{x2-y2} orbitals coupling through in-plane O-$p_{x/y}$ are illustrated in

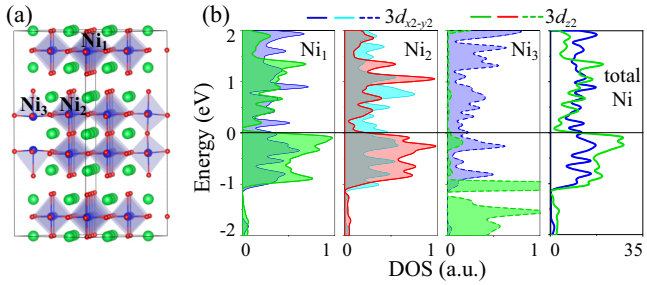

FIG. 15. (a) Schematic crystal structure of the 2×2×1 supercell with one V_{O1} under 20 GPa. (b) Projected DOS for three nonequivalent Ni atoms (left panels), and the sum of DOS for all Ni atoms (right panel).

Figs. 12(a)–12(c). For the case of Ni_1, $t_a^{zx} = t_a^{xz} = 0.24$ eV, and the coupling strengths between d_{z2} and O-p_x ($t_a^{zp} = -0.76$ eV) and between d_{x2-y2} and O-p_x ($t_a^{xp} = -1.61$ eV) are labeled in Fig. 12(a). For the orbitals of Ni_2 and Ni_3 atoms in Figs. 12(b) and 12(c), the coupling strengths t_a^{xp} for Ni_2-d_{x2-y2} (−1.53 eV) and Ni_3-d_{x2-y2} (−1.48 eV) are comparable to that of Ni_1-d_{x2-y2} (−1.61 eV). However, the coupling strength t_a^{zp} for Ni_3-d_{z2} (−0.56 eV) is considerably smaller compared to that of Ni_2-d_{z2} (−0.84 eV) and Ni_1-d_{z2} (−0.76 eV). The reduced coupling strength between Ni_3-d_{z2} and O-p_x is also reflected in the diminished O-$p_{x/y}$ contribution to the Ni_3-d_{z2}-like functions shown in Fig. 4(e). Consequently, this results in a weaker interorbital coupling between Ni_2-d_{x2-y2} and Ni_3-d_{z2} than between Ni_2-d_{z2} and Ni_3-d_{x2-y2}, namely, t_a^{xz} (−0.13 eV) is smaller than t_a^{zx} (−0.21 eV), as given in Figs. 5(e) and 5(f).

Meanwhile, based on the coupling strengths between Ni-d and O-p shown in Figs. 12(a)–12(c), we can roughly infer the indirect coupling between d orbitals along the a axis. For instance, the largest coupling between d_{x2-y2} and O-$p_{x/y}$ results in the largest indirect coupling between NN d_{x2-y2} orbitals ($t_a^x = -0.4$ eV), while the smallest coupling between d_{z2} and $p_{x/y}$ leads to the smallest indirect coupling between NN in-plane d_{z2} orbitals ($t_a^z = -0.1$ eV), as illustrated in Figs. 5(e) and 5(f).

The chemical potential of oxygen is determined by the phase diagram of the R-Ni-O system given in Figs. 6 and 13. It is expected that R327 is stabilized in a chemical-potential region without the formation of all possible competitive phases (e.g., RO_2, R_2O_3, NiO, NiO_2, R_2Ni_7, RNi_5, R_7Ni_{16}, R_3Ni, RNi, R_7Ni_3, etc). The determined chemical-potential region $\Delta\mu$[O] for $La_3Ni_2O_7$, $Ce_3Ni_2O_7$, $Pr_3Ni_2O_7$, and $Nd_3Ni_2O_7$ under 0 GPa is [−0.96, −2.25] eV, [−0.9, −2.31] eV, [−0.95, −2.25] eV, and [−1.05, −2.20] eV, respectively. The chemical potential $\Delta\mu$[O] for $La_3Ni_2O_7$, $Ce_3Ni_2O_7$, $Pr_3Ni_2O_7$, and $Nd_3Ni_2O_7$ under 20 GPa is [0, −2.59] eV, [0, −2.71] eV, [0, −2.58] eV, and [0, −2.40], respectively.

The electronic properties of Pr327 and Nd327 with V_{O1} under 20 GPa are depicted in Fig. 14, exhibiting similar variations to La327. In Fig. 15, the electronic properties of the 2×2×1 supercell with one V_{O1} ($\delta = 0.0625$) under 20 GPa are illustrated. The projected DOS for nonequivalent Ni atoms is similar to the case when $\delta = 0.25$ [see Figs. 2(b)–2(d)].

[1] D. Li, K. Lee, B. Y. Wang, M. Osada, S. Crossley, H. R. Lee, Y. Cui, Y. Hikita, and H. Y. Hwang, Superconductivity in an infinite-layer nickelate, Nature (London) **572**, 624 (2019).

[2] D. Li, B. Y. Wang, K. Lee, S. P. Harvey, M. Osada, B. H. Goodge, L. F. Kourkoutis, and H. Y. Hwang, Superconducting dome in $Nd_{1-x}Sr_xNiO_2$ infinite layer films, Phys. Rev. Lett. **125**, 027001 (2020).

[3] S. Zeng, C. S. Tang, X. Yin, C. Li, M. Li, Z. Huang, J. Hu, W. Liu, G. J. Omar, H. Jani, Z. S. Lim, K. Han, D. Wan, P. Yang, S. J. Pennycook, A. T. S. Wee, and A. Ariando, Phase diagram and superconducting dome of infinite-layer $Nd_{1-x}Sr_xNiO_2$ thin films, Phys. Rev. Lett. **125**, 147003 (2020).

[4] M. Osada, B. Y. Wang, B. H. Goodge, K. Lee, H. Yoon, K. Sakuma, D. Li, M. Miura, L. F. Kourkoutis, and H. Y. Hwang, A superconducting praseodymium nickelate with infinite layer structure, Nano Lett. **20**, 5735 (2020).

[5] M. Osada, B. Y. Wang, Be. H. Goodge, S. P. Harvey, K. O. Lee, D. Li, L. F. Kourkoutis, and H. Y. Hwang, Nickelate superconductivity without rare-earth magnetism: (La, Sr)NiO_2, Adv. Mater. **33**, 45 (2021).

[6] H. Sun, M. Huo, X. Hu, J. Li, Z. Liu, Y. Han, L. Tang, Z. Mao, P. Yang, B. Wang, J. Cheng, D.-X. Yao, G.-M. Zhang, and M. Wang, Signatures of superconductivity near 80 K in a nickelate under high pressure, Nature (London) **621**, 493 (2023).

[7] Y. Zhang, D. Su, Y. Huang, H. Sun, M. Huo, Z. Shan, K. Ye, Z. Yang, R. Li, M. Smidman, M. Wang, L. Jiao, and H. Yuan, High-temperature superconductivity with zero-resistance and strange metal behavior in $La_3Ni_2O_7$, arXiv:2307.14819.

[8] J. Hou, P. T. Yang, Z. Y. Liu, J. Y. Li, P. F. Shan, L. Ma, G. Wang, N. N. Wang, H. Z. Guo, J. P. Sun, Y. Uwatoko, M. Wang, G. M. Zhang, B. S. Wang, and J. G. Cheng, Emergence of high-temperature superconducting phase in the pressurized $La_3Ni_2O_7$ crystals, Chin. Phys. Lett. **40**, 117302 (2023).

[9] G. Wang, N. N. Wang, J. Hou, L. Ma, L. F. Shi, Z. A. Ren, Y. D.Gu, X. L. Shen, H. M. Ma, P. T. Yang, Z. Y. Liu, H. Z. Guo, J. P. Sun, G. M. Zhang, J. Q. Yan, B. S. Wang, Y. Uwatoko, and J.-G. Cheng, Pressure-induced superconductivity in the $La_3Ni_2O_7$-polycrystalline samples, Phys. Rev. X **14**, 011040 (2024).

[10] Y. Zhou, J. Guo, S. Cai, H. Sun, P. Wang, J. Zhao, J. Han, X. Chen, Q. Wu, Y. Ding, M. Wang, T. Xiang, H. Mao, and L. Sun, Evidence of filamentary superconductivity in pressurized $La_3Ni_2O_7$-single crystals, arXiv:2311.12361.

[11] N. N. Wang, M. W. Yang, Z. Yang, K. Y. Chen, H. Zhang, Q. H. Zhang, Z. H. Zhu, Y. Uwatoko, L. Gu, X. L. Dong, J. P. Sun, K. J. Jin, and J.-G. Cheng, Pressure-induced monotonic enhancement of T_c to over 30 K in superconducting $Pr_{0.82}Sr_{0.18}NiO_2$ thin films, Nat. Commun. **13**, 4367 (2022).

[12] Z. Liu, H. Sun, M. Huo, X. Ma, Y. Ji, E. Yi, L. Li, H. Liu, J. Yu, Z. Zhang, Z. Chen, F. Liang, H. Dong, H. Guo, D. Zhong, B. Shen, S. Li, and M. Wang, Evidence for charge and spin density waves in single crystals of $La_3Ni_2O_7$ and $La_3Ni_2O_6$, Sci. China Phys. Mech. Astron. **66**, 217411 (2023).

[13] J. Li, P. Ma, H. Zhang, X. Huang, C. Huang, M. Huo, D. Hu, Z. Dong, C. He, J. Liao, X. Chen, T. Xie, H. Sun, and M. Wang, Pressure-driven dome-shaped superconductivity in bilayer nickelate $La_3Ni_2O_7$, arXiv:2404.11369.

[14] L. Wang, Y. Li, S.-Y. Xie, F. Liu, H. Sun, C. Huang, Y. Gao, T. Nakagawa, B. Fu, B. Dong, Z. Cao, R. Yu, S. I. Kawaguchi, H. Kadobayashi, M. Wang, C. Jin, H. Mao, and H. Liu, Structure responsible for the superconducting state in $La_3Ni_2O_7$ at high pressure and low temperature conditions, arXiv:2311.09186.

[15] C. Lu, Z. Pan, F. Yang, and C. Wu, Interlayer coupling driven high-temperature superconductivity in $La_3Ni_2O_7$ under pressure, Phys. Rev. Lett. **132**, 146002 (2024).

[16] Y. Cao and Y.-F. Yang, Flat bands promoted by Hund's rule coupling in the candidate double-layer high-temperature superconductor $La_3Ni_2O_7$, Phys. Rev. B **109**, L081105 (2024).

[17] Z. Luo, X. Hu, M. Wang, W. Wu, and D.-X. Yao, Bilayer two-orbital model of $La_3Ni_2O_7$ under pressure, Phys. Rev. Lett. **131**, 126001 (2023).

[18] Y. Zhang, L.-F. Lin, A. Moreo, and E. Dagotto, Electronic structure, orbital-selective behavior, and magnetic tendencies in the bilayer nickelate superconductor $La_3Ni_2O_7$ under pressure, Phys. Rev. B **108**, L180510 (2023).

[19] H. Sakakibara, N. Kitamine, M. Ochi, and K. Kuroki, Possible high T_c superconductivity in $La_3Ni_2O_7$ under high pressure through manifestation of a nearly-half-filled bilayer Hubbard model, Phys. Rev. Lett. **132**, 106002 (2024).

[20] Y. Gu, C. Le, Z. Yang, X. Wu, and J. Hu, Effective model and pairing tendency in bilayer Ni-based superconductor $La_3Ni_2O_7$, arXiv:2306.07275.

[21] D.-C. Lu, M. Li, Z.-Y. Zeng, W. Hou, J. Wang, F. Yang, and Y.-Z. You, Superconductivity from doping symmetric mass generation insulators: Application to $La_3Ni_2O_7$ under pressure, arXiv:2308.11195.

[22] W. Wu, Z. Luo, D.-X. Yao, and M. Wang, Charge transfer and Zhang-Rice singlet bands in the nickelate superconductor $La_3Ni_2O_7$ under pressure, Sci. China Phys. Mech. Astron. **67**, 117402 (2024).

[23] Y. Shen, M. Qin, and G.-M. Zhang, Effective bi-layer model Hamiltonian and density-matrix renormalization group study for the high-T_c superconductivity in $La_3Ni_2O_7$ under high pressure, Chin. Phys. Lett. **40**, 127401 (2023).

[24] Y. Yang, G.-M. Zhang, and F.-C. Zhang, Minimal effective model and possible high-T_c mechanism for superconductivity of $La_3Ni_2O_7$ under high pressure, Phys. Rev. B **108**, L201108 (2023).

[25] J. Chen, F. Yang, and W. Li, Orbital-selective superconductivity in the pressurized bilayer nickelate $La_3Ni_2O_7$: An infinite projected entangled-pair state study, arXiv:2311.05491.

[26] X.-Z. Qu, D.-W. Qu, J. Chen, C. Wu, F. Yang, W. Li, and G. Su, Bilayer t-J-$J^{\perp}$ model and magnetically mediated pairing in the pressurized nickelate $La_3Ni_2O_7$, Phys. Rev. Lett. **132**, 036502 (2024).

[27] Q. -G. Yang, D. Wang, and Q.-H. Wang, Possible $s^{\pm}$-wave superconductivity in $La_3Ni_2O_7$, Phys. Rev. B **108**, L140505 (2023).

[28] Y.-B. Liu, J.-W. Mei, F. Ye, W.-Q. Chen, and F. Yang, The $s^{\pm}$-wave pairing and the destructive role of apical-oxygen deficiencies in $La_3Ni_2O_7$ under pressure, Phys. Rev. Lett. **131**, 236002 (2023).

[29] Y. Zhang, L.-F. Lin, A. Moreo, T. A. Maier, and E. Dagotto, Structural phase transition, $s^{\pm}$-wave pairing and magnetic stripe order in the bilayered nickelate superconductor $La_3Ni_2O_7$ under pressure, Nat. Commun. **15**, 2470 (2024).

[30] Y. Zhang, L.-F. Lin, A. Moreo, T. A. Maier, and E. Dagotto, Trends in electronic structures and $s^{\pm}$-wave pairing for the rare-earth series in bilayer nickelate superconductor $R_3Ni_2O_7$, Phys. Rev. B **108**, 165141 (2023).

[31] H. Oh and Y. H. Zhang, Type II t-J model and shared antiferromagnetic spin coupling from Hund's rule in superconducting $La_3Ni_2O_7$, Phys. Rev. B **108**, 174511 (2023).

[32] Z. Liao, L. Chen, G. Duan, Y. Wang, C. Liu, R. Yu, and Q. Si, Electron correlations and superconductivity in $La_3Ni_2O_7$ under pressure tuning, arXiv:2307.16697.

[33] F. Lechermann, J. Gondolf, S. Bötzel, and I. M. Eremin, Electronic correlations and superconducting instability in $La_3Ni_2O_7$ under high pressure, Phys. Rev. B **108**, L201121 (2023).

[34] V. Christiansson, F. Petocchi, and P. Werner, Correlated electronic structure of $La_3Ni_2O_7$ under pressure, Phys. Rev. Lett. **131**, 206501 (2023).

[35] Z. Liu, M. Huo, J. Li, Q. Li, Y. Liu, Y. Dai, X. Zhou, J. Hao, Y. Lu, M. Wang, and W.-H. Wen, Electronic correlations and energy gap in the bilayer nickelate $La_3Ni_2O_7$, arXiv:2307.02950.

[36] D. A. Shilenko and I. V. Leonov, Correlated electronic structure, orbital-selective behavior, and magnetic correlations in double-layer $La_3Ni_2O_7$ under pressure, Phys. Rev. B **108**, 125105 (2023).

[37] Z. Dong, M. Huo, J. Li, J. Li, P. Li, H. Sun, Y. Lu, M. Wang, Y. Wang, and Z. Chen, Visualization of oxygen vacancies and self-doped ligand holes in $La_3Ni_2O_{7-\delta}$, arXiv:2312.15727.

[38] G. Xiao, M. Z. Cieplak, A. Gavrin, F. H. Streitz, A. Bakhshai, and C. L. Chien, High-temperature superconductivity in tetragonal perovskite structures: Is oxygen-vacancy order important? Phys. Rev. Lett. **60**, 1446 (1988).

[39] C. L. Jia, M. Lentzen, and K. Urban, Atomic-resolution imaging of oxygen in perovskite ceramics, Science **299**, 870 (2003).

[40] A. R. Puigdollers, P. Schlexer, S. Tosoni, and G. Pacchioni, Increasing oxide reducibility: The role of metal/oxide interfaces in the formation of oxygen vacancies, ACS Catal. **7**, 6493 (2017).

[41] M. T. Greiner, L. Chai, M. G. Helander, W.-M. Tang, and Z.-H. Lu, Transition metal oxide work functions: The influence of cation oxidation state and oxygen vacancies, Adv. Funct. Mater. **22**, 4557 (2012).

[42] J. Kim, X. Yin, K.-C. Tsao, S. Fang, and H. Yang, $Ca_2Mn_2O_5$ as oxygen-deficient perovskite electrocatalyst for oxygen evolution reaction, J. Am. Chem. Soc. **136**, 14646 (2014).

[43] Q. Ji, L. Bi, J. Zhang, H. Cao, and X. S. Zhao, The role of oxygen vacancies of ABO_3 perovskite oxides in the oxygen reduction reaction, Energy Environ. Sci. **13**, 1408 (2020).

[44] W. Hou, P. Feng, X. Guo, Z. Wang, Z. Bai, Y. Bai, G. Wang, and K. Sun, Catalytic mechanism of oxygen vacancies in perovskite oxides for lithium-sulfur batteries, Adv. Mater. **34**, 2202222 (2022).

[45] Z. Zhang, M. Greenblatt, and J. B. Goodenough, Synthesis, structure, and properties of $Ln_4Ni_3O_{10-\delta}$ (Ln = La, Pr, and Nd), J. Solid State Chem. Solids. **108**, 402 (1994).

[46] S. Taniguchi, T. Nishikawa, Y. Yasui, Y. Kobayashi, J. Takeda, S. Shamoto, and M. Sato, Transport, magnetic and thermal properties of $La_3Ni_2O_{7-\delta}$, J. Phys. Soc. Jpn. **64**, 1644 (1995).

[47] M. Greenblatt, Z. Zhang, and M. H. Whangbo, Electronic properties of $La_3Ni_2O_7$ and $Ln_4Ni_3O_{10}$, Ln = La, Pr and Nd, Synth. Met. **85**, 1451 (1997).

[48] P. H. Hor, R. L. Meng, Y. Q. Wang, L. Gao, Z. J. Huang, J. Bechtold, K. Forster, and C. W. Chu, Superconductivity above 90 K in the square-planar compound system $ABa_2Cu_3O_{6+x}$ with $A = Y$, La, Nd, Sm, Eu, Gd, Ho, Er and Lu, Phys. Rev. Lett. **58**, 1891 (1987).

[49] G. Wang, N. N. Wang, Y. X. Wang, L. F. Shi, X. L. Shen, J. Hou, H. M. Ma, P. T. Yang, Z. Y. Liu, H. Zhang, X. L. Dong, J. P. Sun, B. S. Wang, K. Jiang, J. P. Hu, Y. Uwatoko, and J.-G. Cheng, Observation of high-temperature superconductivity in the high-pressure tetragonal phase of $La_2PrNi_2O_{7-\delta}$, arXiv:2311.08212.

[50] B. Geisler, J. J. Hamlin, G. R. Stewart, R. G. Hennig, and P. J. Hirschfeld, Structural transitions, octahedral rotations, and electronic properties of $A_3Ni_2O_7$ rare-earth nickelates under high pressure, npj Quantum Mater. **9**, 38 (2024).

[51] B. Geisler, L. Fanfarillo, J. J. Hamlin, G. R. Stewart, R. G. Hennig, and P. J. Hirschfeld, Optical properties and electronic correlations in $La_3Ni_2O_7$ bilayer nickelates under high pressure, arXiv:2401.04258.

[52] G. Kresse and J. Furthmuller, Efficient iterative schemes for ab initio total-energy calculations using a plane-wave basis set, Phys. Rev. B **54**, 11169 (1996).

[53] G. Kresse and D. Joubert, From ultrasoft pseudopotentials to the projector augmented-wave method, Phys. Rev. B **59**, 1758 (1999).

[54] D. Vanderbilt, Soft self-consistent pseudopotentials in a generalized eigenvalue formalism, Phys. Rev. B **41**, 7892 (1990).

[55] J. P. Perdew, K. Burke, and M. Ernzerhof, Generalized gradient approximation made simple, Phys. Rev. Lett. **77**, 3865 (1996).

[56] P. E. Blöchl, Projector augmented-wave method, Phys. Rev. B **50**, 17953 (1994).

[57] S. Baroni, P. Giannozzi, and A. Testa, Green's-function approach to linear response in solids, Phys. Rev. Lett. **58**, 1861 (1987).

[58] X. Gonze, Adiabatic density-functional perturbation theory, Phys. Rev. A **52**, 1096 (1995).

[59] L. Chaput, A. Togo, I. Tanaka, and G. Hug, Phonon-phonon interactions in transition metals, Phys. Rev. B **84**, 094302 (2011).

[60] A. Togo and I. Tanaka, First principles phonon calculations in materials science, Scr. Mater. **108**, 1 (2015).

[61] K. Parlinski, Z. Q. Li, and Y. Kawazoe, First-principles determination of the soft mode in cubic ZrO_2, Phys. Rev. Lett. **78**, 4063 (1997).

[62] A. A. Mostofi, J. R. Yates, G. Pizzi, Y.-S. Lee, I. Souza, D. Vanderbilt, and N. Marzari, An updated version of wannier90: A tool for obtaining maximally-localized Wannier functions, Comput. Phys. Commun. **185**, 2309 (2014).

[63] J. Yang, H. Sun, X. Hu, Y. Xie, T. Miao, H. Luo, H. Chen, B. Liang, W. Zhu, G. Qu, C.-Q. Chen, M. Huo, Y. Huang, S. Zhang, F. Zhang, F. Yang, Z. Wang, Q. Peng, H. Mao, G. Liu, Z. Xu, T. Qian, D.-X. Yao, M. Wang, L. Zhao, and X. J. Zhou, Orbital-dependent electron correlation in double-layer nickelate $La_3Ni_2O_7$, arXiv:2309.01148.

[64] V. I. Anisimov, J. Zaanen, and O. K. Anderson, Band theory and Mott insulators: Hubbard U instead of Stoner *I*, Phys. Rev. B **44**, 943 (1991).

[65] H. LaBollita, V. Pardo, M. R. Norman, and A. S. Botana, Electronic structure and magnetic properties of $La_3Ni_2O_7$ under pressure: The active role of the Ni-d_{x2-y2} orbitals, arXiv:2309.17279.

[66] N. Marzari, A. A. Mostofi, J. R. Yates, I. Souza, and D. Vanderbilt, Maximally localized Wannier functions: Theory and applications, Rev. Mod. Phys. **84**, 1419 (2012).

[67] N. Hatada, Chesta-software for creating chemical potential diagrams, https://n-hatada.github.io/chesta.

[68] L. C. Rhodes and P. Wahl, Structural routes to stabilize superconducting $La_3Ni_2O_7$ at ambient pressure, Phys. Rev. Mater. **8**, 044801 (2024).

[69] R. Jacobs, G. Luo, and D. Morgan, Materials discovery of stable and nontoxic halide perovskite materials for high-efficiency solar cells, Adv. Funct. Mater. **29**, 1804354 (2019).

[70] C. J. Bartel, J. M. Clary, C. Sutton, D. Vigil-Fowler, B. R. Goldsmith, A. M. Holder, and C. B. Musgrave, Inorganic halide double perovskites with optoelectronic properties modulated by sublattice mixing, J. Am. Chem. Soc. **142**, 5135 (2020).

[71] G. Wu, J. J. Neumeier, and M. F. Hundley, Magnetic susceptibility, heat capacity, and pressure dependence of the electrical resistivity of $La_3Ni_2O_7$ and $La_4Ni_3O_{10}$, Phys. Rev. B **63**, 245120 (2001).

[72] K. Chen, X. Liu, J. Jiao, M. Zou, Y. Luo, Q. Wu, N. Zhang, Y. Guo, and L. Shu, Evidence of spin density waves in $La_3Ni_2O_{7-\delta}$, arXiv:2311.15717.

[73] L. Wang, Y. Li, S.-Y. Xie, F. Liu, H. Sun, C. Huang, Y. Gao, T. Nakagawa, B. Fu, B. Dong, Z. Cao, R. Yu, S. I. Kawaguchi, H. Kadobayashi, M. Wang, C. Jin, H. Mao, and H. Liu, Structure responsible for the superconducting state in $La_3Ni_2O_7$ at high-pressure and low-temperature conditions, J. Am. Chem. Soc. **146**, 7506 (2024).

[74] X.-W. Yi, Y. Meng, J.-W. Li, Z.-W. Liao, J.-Y. You, B. Gu, and G. Su, Antiferromagnetic ground state, charge density waves and oxygen vacancies induced metal-insulator transition in pressurized $La_3Ni_2O_7$, arXiv:2403.11455.

Correction: A second affiliation was inadvertently added to the fifth author and has been fixed.